J. Fluid Mech. (2008), *vol.* 610, *pp.* 157–182.
doi:10.1017/S002211200800253X Printed in the United Kingdom

The acceleration of solid particles subjected to cavitation nucleation

BRAM M. BORKENT[1], MANISH ARORA[1], CLAUS-DIETER OHL[1,2], NICO DE JONG[1], MICHEL VERSLUIS[1], DETLEF LOHSE[1], KNUD AAGE MØRCH[3], EVERT KLASEBOER[4] AND BOO CHEONG KHOO[5]

[1]Physics of Fluids, Faculty of Science and Technology, University of Twente, Postbus 217, 7500 AE Enschede, The Netherlands

[2]Division of Physics and Applied Physics, School of Physical and Mathematical Sciences, Nanyang Technological University, 21 Nanyang Link, Singapore 637371

[3]Department of Physics and Center of Quantum Protein, Technical University of Denmark, DK-2800 Kgs. Lyngby, Denmark

[4]Institute of High Performance Computing, Science Park Road, #01-01 The Capricorn, Singapore Science Park II, Singapore 117528

[5]Department of Mechanical Engineering, National University of Singapore, 10 Kent Ridge Crescent, Singapore 119260

(Received 29 April 2007 and in revised form 20 May 2008)

The cavity–particle dynamics at cavitation inception on the surface of spherical particles suspended in water and exposed to a strong tensile stress wave is experimentally studied with high-speed photography. Particles, which serve as nucleation sites for cavitation bubbles, are set into a fast translatory motion during the explosive growth of the cavity. They reach velocities of $\sim 40\,\mathrm{m\,s^{-1}}$ and even higher. When the volume growth of the cavity slows down, the particle detaches from the cavity through a process of neck-breaking, and the particle is shot away. The experimental observations are simulated with (i) a spherical cavity model and (ii) with an axisymmetric boundary element method (BEM). The input for both models is a pressure pulse, which is obtained from the observed radial cavity dynamics during an individual experiment. The model then allows us to calculate the resulting particle trajectory. The cavity shapes obtained from the BEM calculations compare well with the photographs until neck formation occurs. In several cases we observed inception at two or more locations on a single particle. Moreover, after collapse of the primary cavity, a second inception was often observed. Finally, an example is presented to demonstrate the potential application of the cavity–particle system as a particle cannon, e.g. in the context of drug delivery into tissue.

1. Introduction

The tensile strength of a liquid is the stress it can resist before it ruptures. For pure water, homogeneous nucleation theory predicts a threshold of -140 MPa at $25\,^{\circ}\mathrm{C}$ before cavities form. Although this high threshold has been verified for pristine water trapped in minerals (Green *et al.* 1990; Zheng *et al.* 1991), ultimate thresholds being a factor 10 smaller are reported even in very pure water. Harvey *et al.* (1944) attributed the measured low tensile strength of plain water to cavitation nuclei, stabilized in crevices at solid surfaces, and Atchley & Prosperetti (1989) developed a quantitative

model for the bubble dynamics in crevices. Subsequent investigations (Greenspan & Tschiegg 1967; Apfel 1970; Madanshetty 1995; Mørch 2000; Holmberg *et al.* 2003; Marschall *et al.* 2003) have supported the basic character of cavitation nuclei as interfacial voids, though not necessarily located at crevices. Recently Arora, Ohl & Mørch (2004) documented the inception process on corrugated spherical polystyrene particles. Their high-speed photo sequences showed that when subjected to a tensile stress wave, solid particles with diameters in the 30–150 μm range nucleated cavities which grew to sizes much larger than the particles themselves. The particles were observed to move away at high speed, typically in the 10 m s^{-1} range, from the cavities they themselves nucleated. The connection between the cavity and the nucleating particle was broken within about 10 μs, and thereafter the detached particle was translated independent of the cavity. Though it is well known that normal liquids contain large numbers of small particles, and that they are of importance for cavitation inception (Crum 1979), the complex sequence of events at inception may explain the difficulties experienced over the years in understanding the phenomenon.

The present work is motivated by the demand for a deeper analysis of this basic mechanism of cavitation inception, experimentally as well as theoretically. Arora *et al.* (2004) triggered their cavitation events by the negative phase of the pressure pulse from a lithotripter, and recorded them with photographic equipment that allowed only two frames to be captured in each experimental run. Though the principal features of the process were clear, details of the dynamics were not revealed, and the theory presented requires adjustment in order to give quantitatively correct particle motion data for comparison with experiments.

Such analysis may contribute to explaining, for example, the finding that particle-laden flows cause accelerated surface erosion (Madadnia & Owen 1993, 1995) at low pressure/cavitation conditions, way beyond the added effects of simple particle erosion and cavitation erosion. It has been suggested that particles are propelled towards solid surfaces by the jetting mechanism of collapsing cavitation bubbles, thus causing erosion on impact. However, experiments with particles positioned close to a spark-induced cavitation bubble showed little motion during its expansion and collapse (Soh & Willis 2003). Therefore, it is inferred that particles cannot just be propelled by cavity-induced flow onto a solid wall, such that they cause wear at collision. In contrast, we find that particle acceleration to considerable speed is achieved when cavities are nucleated and grow from the surface of particles exposed to tensile stress, thus offering a possible mechanism of wear.

In the present work, we first present the experimental set-up for initiating and recording cavitation on suspended particles. In contrast to the earlier works, we now record the dynamics with much higher temporal resolution. We have 128 consecutive frames in high-speed recordings at up to a million frames per second to study the inception in detail. Then we present characteristic examples of cavitation events on a particle, and distinguish three different dynamic regimes. Two theoretical models based on potential theory are presented, one with direct calculations of the particle–cavity interaction using the pressure gradient along the particle surface, the other using the boundary-element method. Both models are able to predict very well the phenomena observed in the experiments.

2. Experimental set-up

The experimental set-up is shown in figure 1. Dry polystyrene particles (polystyrene-2% divinylbenzene, with a diameter distribution 30–150 μm and of

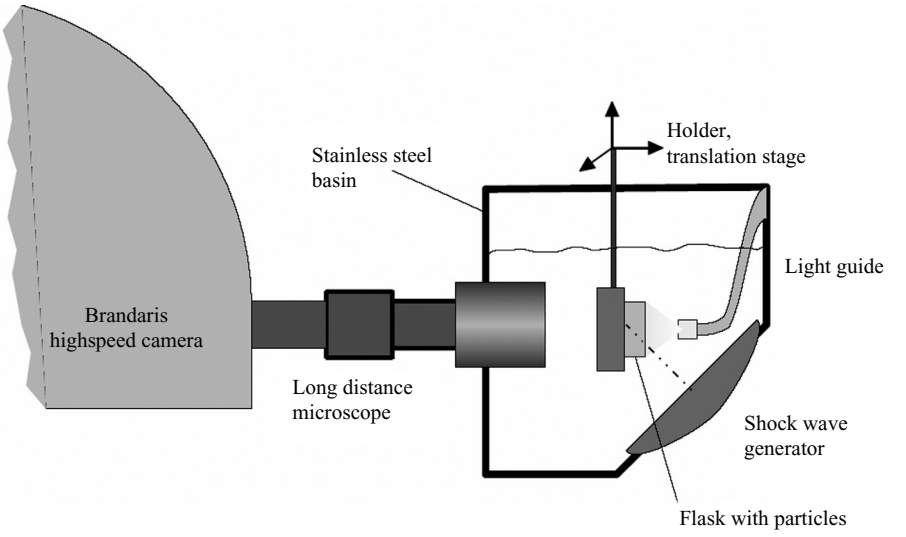

FIGURE 1. Sketch of the experimental set-up. The particles are suspended in a flask which can be positioned in the water basin with a three-axis translation stage. The pressure wave is generated with the shock wave generator from a commercial lithotripter. A light guide serves as back illumination for the high-speed camera, which is connected to a long distance microscope observing the particles. The thickness of the flask is 20 mm and the distance between the glass surface protecting the long distance microscope and the flask is ~30 mm. The water level is about 100 mm above the acoustic focus.

density $\rho_p = 1.05 \times 10^3\,\mathrm{kg\,m^{-3}}$) of spherical shape and with nano-scale surface roughness (Marschall *et al.* 2003; Arora *et al.* 2004; Borkent, Arora & Ohl 2007; Mørch 2007) were suspended in partly degassed water from a Milli-Q water-purification system, contained in a sterile flask (75 ml Nunc EasyFlask, Nunclon). The closed flask, containing $\sim 1 \times 10^4$ particles, was submerged into a basin with approximately 50 l of de-mineralized water. A waterproof magnetic stirrer (Telemodul 90407, Variomag) drove a glass-encapsulated magnet within the flask to prevent sedimentation of the particles. In the selection of particles, we noticed that their size matters. Spherical polyamide particles of a density the same as the polystyrene particles, but of a diameter of only 20 μm, could not be propelled away by cavitation nucleation. We argue that this is an effect of their limited size, causing drag to dominate. In addition, the pressure drop across their surface is relatively small and the particles are not able to acquire enough momentum.

Heterogeneous cavitation on the particles was excited with a focused wave from a slightly modified commercial shock-wave lithotripter (Piezolith 3000, Richard-Wolf GmbH, Knittlingen, Germany). The transducer consisted of two active layers, each with hundreds of piezoelectric ceramics arranged in a hexagonal pattern and wired in parallel, on the front and back sides, respectively, of a spherically shaped shell. The clinical device has a fixed delay between the two layers, which ensures that the pressure waves emitted from both layers superimpose constructively. However, in our set-up we could control both layers individually in time and driving voltage. If not mentioned otherwise, only the frontal transducer was operated, and at a discharge voltage of 5 kV. The transducer had a diameter of 251 mm and an opening angle of 94°.

In figure 2, a typical pressure recording is shown, as obtained with a calibrated glass fibre hydrophone (FOPH-500, RP Acoustics). It was positioned inside the flask, close

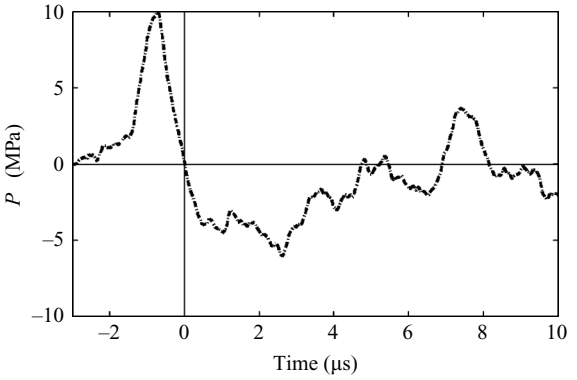

FIGURE 2. Typical pressure profile in water without particles seeded into the liquid, measured in a single experiment as a function of time. The measured negative part lasts roughly 5 μs and reaches a value of about −6 MPa. When particles are present cavitation occurs during the negative part of the pressure pulse, i.e. for $t > 0$, and it affects the pulse shape. A pressure profile with a longer temporal duration of 40 μs is presented in Arora *et al.* 2004.

to the acoustic focus, which was marked with two crossed beams from laser diodes. The Milli-Q water in the flask did not contain particles and it therefore showed low cavitation activity. The travelling time of the pressure wave from the surface of the frontal transducer to the acoustic focus was ∼136 μs which was important for the time-delay used for the flashlight and camera. The wave path via the closest reflecting object (the wall of the flask) to the acoustic focus corresponded to a delay of ∼7 μs, but as any tensile stress pulse, that was strong enough to cause cavitation served our purpose, reflections were in principle without importance. In the recorded lithotripter pulse (figure 2) the pressure first rose to a positive peak pressure of about 10 MPa, and then it dropped to –6 MPa. The pressure varied strongly with the spatial position owing to the narrow focal width, being only 1.8 mm at half of the maximum pressure amplitude. The period of tensile stress was responsible for the creation of cavitation bubbles when the particles were seeded into the water. In experiments with particles, the local pressure at the focal region differs from that shown in figure 2 owing to the expansion and collapse of neighbouring cavities. A shortening of the tensile stress pulse occurs at high cavitation activity when many cavities form (Pishchalnikov *et al.* 2005; Liebler, Dreyer & Riedlinger 2006; Arora, Ohl & Lohse 2007). Additionally, when cavitation sets in, the pressure measurements obtained with a fibreoptic hydrophone vary considerably from shot to shot owing to the statistical nature of the bubble dynamics in the whole cavitation zone. Zijlstra & Ohl (2008) found that the pressure fluctuations are real, and caused by acoustic transients emitted from nearby cavitation bubbles. Owing to the statistical nature of the local pressure during cavitation, only a typical pressure pulse measurement in a non-cavitating liquid (i.e. without particles) is presented. It was impossible to record the pressure at exactly the position of the particle being observed to cavitate, as all the particles were moving freely, and we had no control over their positions or of which ones would cause cavitation in the experiment. Even if we did try, we had measured at best a pressure that was not necessarily the far-field pressure in a 'Rayleigh sense', but just a local pressure. Further, the probe itself would have disturbed the event being studied. Thus, we could not expect that a measured pressure would be representative of the observed bubble expansion. Instead we have used the observed cavity dynamics as our local pressure probe. It is this dynamics that governs the specific particle motion

being recorded in the experiment, and which we aim to calculate. This is probably the only way to obtain the 'far-field pressure' of an observed cavity. The technique is applicable only with a sufficiently high resolution both in time and space.

Microscopic imaging of particles and cavitation bubbles from a distance of 40 mm was done with a long-working-distance objective (K2, C4 objective, Infinity, USA) illuminated with a continuous light source from behind. For recording of the fast dynamics with a sufficient number of frames, we used the rotating mirror camera Brandaris-128 equipped with 128 light-sensitive image sensors which were read out digitally (Chin *et al.* 2003). Although the camera can be operated with up to 25 million frames per second we used up to 10^6 frames s^{-1} only, to gain longer recording times. After each experiment, the images were transferred to a computer and corrected for slight misalignments of the individual sensors, using digital image-processing routines. Finally, a movie with 128 frames, each of 475×346 pixels and with a resolution of 5.7 μm $pixel^{-1}$, was stored.

In the experimental procedure, the camera was operated as the master device, which triggered the shock-wave generator 136 μs before the first frame of the sequence was to be recorded. Within this time interval the pressure wave travelled from the surface of the transducer to the centre of the flask.

Not every experimental run led to a movie with particles in focus because the particles were randomly mixed in the flask. By adjusting the particle concentration, we obtained one or more particles imaged in focus in about a third of the experiments. Altogether, 51 recordings with a single pressure pulse and 105 recordings with two shock waves at different delay settings were found to be suited for further analysis.

Because the particle motion is not limited to the image plane, the measured positions are only projections onto the image plane, and thus the experimentally determined velocities are lower bounds. Yet, the focal depth of the long-distance microscope of $\sim$50 μm causes a blurring of particles leaving the focal plane. The typical travel distance of particles being imaged in focus during their entire motion is 300 μm–400 μm, and thus much larger than the focal depth. In two of the three cases presented in this paper, we can consider the motion to be fairly close to the image plane.

Finally, the sizes of the objects of interest (the particle and the cavity) are determined as follows. The contour of the object of interest is identified manually with 5 points. Through these points a circular fit is calculated, giving the corresponding area and hence the radius of the object. Comparing the calculated size of the particle in all the frames, which should be constant, we find that the absolute error in the experimental data is less than 3 μm.

3. Experimental observations

A typical and instructive recording that shows cavitation inception on a particle of radius $R_p = 68$ μm is presented in figure 3. In the first frame, the tensile stress pulse has arrived, and from time $t = 1.0$ μs to $t = 2.9$ μs a cavity grows from a point on the particle surface with a radial expansion velocity of about 70 m s^{-1}. Its radius reaches a maximum of 203 μm and it becomes approximately spherical, but it only partly entrains the particle. In the following frames the remarkable dynamics is revealed ($t = 2.9$–10.8 μs): the particle moves away from the cavity wall, shaping first a neck which connects it to the cavity, but eventually the neck breaks. The particle velocity, v_p, comes up to a maximum of 37 m s^{-1} at $t = 2.9$ μs, and then drops to 15 m s^{-1} at $t = 10.8$ μs. From this time, the particle moves along independently, completely free

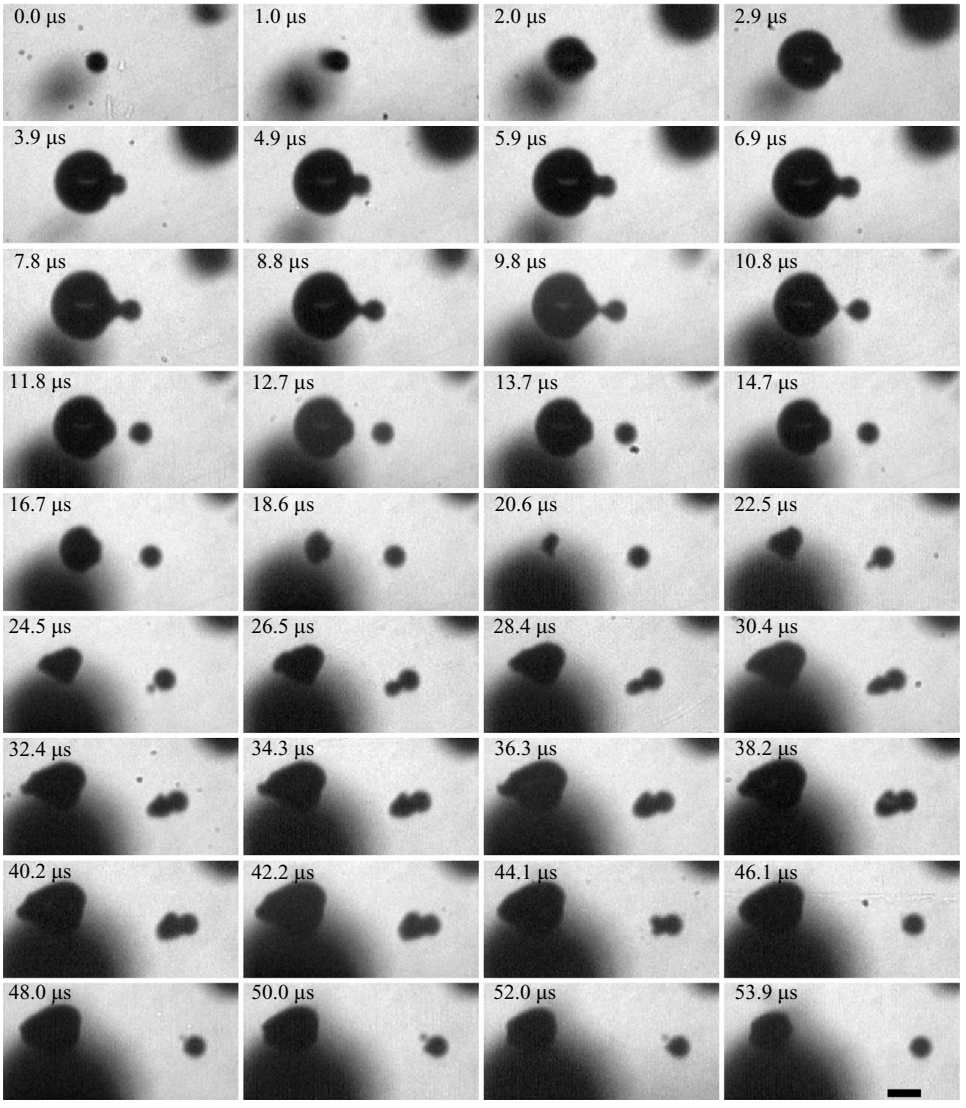

FIGURE 3. Example of a cavitation event on a particle and the successive dynamics. In the first frame, $t = 0$, an isolated particle is visible. A cavitation bubble expanding on the left-hand side of the particle becomes visible at $t = 1\,\mu s$ and grows explosively. As the growth decelerates ($t = 4.9\,\mu s$), the particle moves away from the cavity and forms a neck which breaks around $t = 10.8\,\mu s$. During the detachment process, the cavity develops a mushroom shape, and collapses between $t = 18.6\,\mu s$ and $t = 20.6\,\mu s$. Moreover, the volume centre of the cavity shifts slightly to the left. The re-expanding cavity obtains a funnel-like shape, which indicates that a liquid jet has developed during the cavity collapse. A secondary attached cavity on the particle becomes visible at $t = 20.6\,\mu s$ and grows in the following frames into a void of size comparable to that of the particle. The black bar in the last frame has a length of $200\,\mu m$. Two additional out-of-focus cavitation events are recorded in this series, too. They are visible as blurred shadows, one in the upper right-hand corner and the other as a dark fuzzy object just below the in-focus cavity. Movie 1 is available with the online version of the paper.

of the cavity, which shrinks and reaches a minimum size at $t = 19.6\,\mu s$ (not shown). Then the cavity re-expands while its centre moves slightly in the direction opposite that of the particle, and it develops a protrusion directed away from the particle.

Most probably, the protrusion is caused by a liquid jet flow through the centre of the cavity, deforming the opposite cavity surface on impact. From $t = 22.5\,\mu s$ to $34.3\,\mu s$ a new attached cavity grows on the downstream side of the particle. This is primarily interesting from an inception point of view because in our experiments the first and primary cavity develops from a nucleus of strongly negative critical pressure (-2 to -3 MPa), while the secondary cavity develops unexpectedly, and at a pressure close to zero.

We can separate the dynamics depicted in figure 3 into three regimes.

(i) Explosive bubble growth on the particle ($t = 0$–$4.9\,\mu s$).

(ii) Neck formation and detachment of the particle ($t = 4.9$–$10.8\,\mu s$).

(iii) Collapse and re-expansion of the cavity, and growth of a secondary attached cavity from the particle.

The ejection of the particle from the cavity is due to momentum being imparted to it by the pressure drop that arises across it when a sufficient tensile stress in the liquid causes cavitation inception at the particle surface. The surface area of the particle in contact with the cavity then experiences the vapour pressure, while at inception and just after inception the opposite side is exposed to a pressure governed by the tensile stress of the lithotripter pulse. Hence the particle is accelerated away from the position of cavity nucleation. When the tensile stress in the pulse relaxes and the pressure becomes positive, the cavity growth decelerates, and eventually the cavity shrinks and collapses. In contrast, the particle continues to move with the velocity gained, it separates from the cavity, and moves on until viscous forces stop its motion.

3.1. *Single and multiple cavity events*

In 40 of the 51 recordings with a single pressure pulse, the growth of a single cavity on the particle is observed. In the remaining 11 experiments, we find two or more cavities growing explosively from a single particle. Figure 4 depicts such a case of multiple cavitation inception occurring on two particles in the field of view during the initial $8\,\mu s$. On inspection of the images, four exploding cavitation bubbles can be distinguished on the lower right particle in figure 4 at $8.2\,\mu s$. The liquid space separating the two uppermost cavities on this particle remains visible until $t = 4.1\,\mu s$. At $t = 5.1\,\mu s$, it disappears, but at its former position a swelling of the merging cavity surfaces starts, and in the successive frames a bulge grows. The arrows in figure 4 point at former liquid films between cavities, which have transformed into swelling interfaces. The upper left particle in figure 4 also seems to develop four cavities at $t = 1.0\,\mu s$. The three lower ones merge without the process being visible, while the upper one clearly merges with the lower ones at $t = 4.1\,\mu s$. From the geometry it seems that after the merging, the bulge is located circumferentially. Thus, the two bulges marked with the uppermost arrows in figure 4 result from the merging of a cavity with a system of neighbouring cavities. The swelling of an interface has been reported as an indication for coalescence in experiments by Lal & Menon (1996), and in numerical simulations by Rungsiyaphornrat *et al.* (2003).

3.2. *Non-depletion of cavitation nuclei*

Can cavitation bubbles be nucleated multiple times from the same particle? Though the depletion of cavitation activity has been observed by Borkent *et al.* (2007), where they show that cavitation nuclei become finally used up when repetitive pulses are applied, this does not necessarily mean that particles cannot nucleate multiple times. To test this experimentally we exposed particles to two successive shock waves within a sufficiently short interval of time. We found that a time interval of $200\,\mu s$ allowed the cavitation dynamics from the first tensile wave to cease, so that no visible cavities

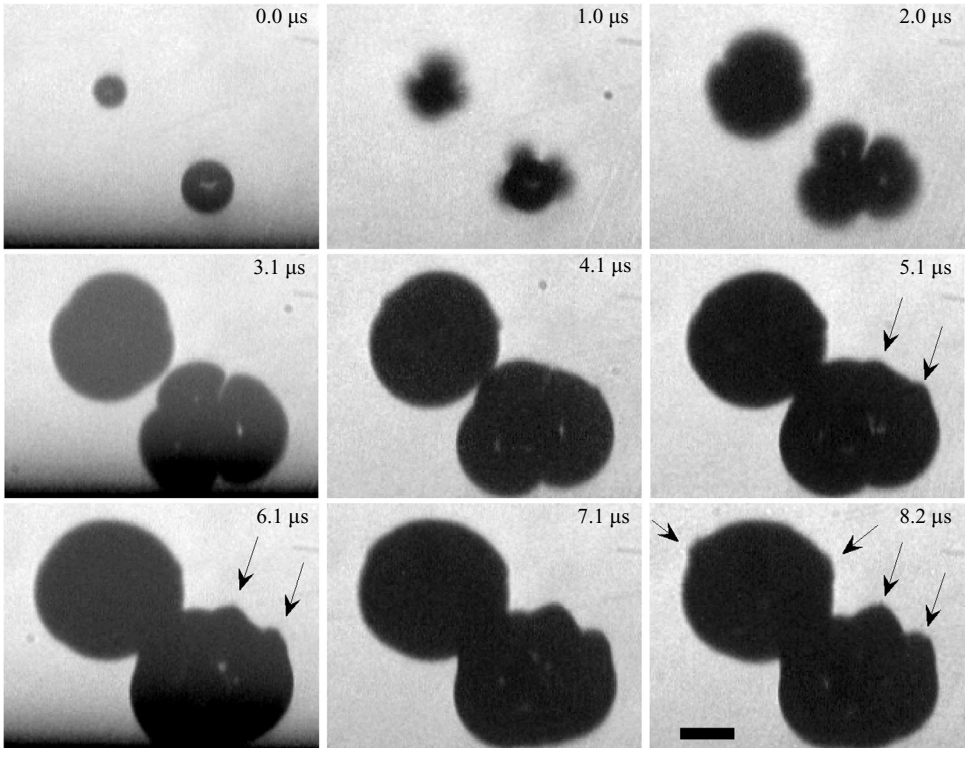

FIGURE 4. Multiple cavitation inception sites are found on particles in about 20 % of the experimental runs. Here, two particles which both show multiple cavity growth on their surface are depicted. When the cavities merge (between 4.1 μs and 5.1 μs) swelling of the gas–liquid interface occurs, which is indicated with arrows. The scale bar in the last frame is 200 μm in length.

remained. Yet, particles accelerated by cavitation inception at the first wave had still not left the field of view. The design of the shock wave source allowed both piezoelectric layers to be triggered independently. Here, the frontal layer was used for the first shock wave, and the back layer for the second. When the camera was operated at framing rates below 0.30×10^6 frames s^{-1} the cavitation dynamics from both shock waves could be captured in a single recording.

From a total number of 92 recordings showing cavitation activity on a particle at exposure to the first shock wave, 23 recordings revealed cavitation activity again on the same particle after the second shock-wave exposure. Thirty-four recordings showed no second cavitation event on the particle, whereas in the remaining cases it was impossible to see what happened, owing to particles moving out of the screen, motion blurring, or cavitation bubbles that were too large. An example of two-fold cavitation activity on the same particle is depicted in figure 5 where the camera was operated at a framing rate of 0.28×10^6 frames s^{-1}. Close to $t = 0.0$ μs the negative part of the shock wave impacts the particle imaged in focus, and makes a cavity grow on its surface. At $t = 7.4$ μs, the particle splits from the cavitation bubble, leaving a short neck, and the particle moves upward with a small tilt to the left. During the detachment process, an elongated attached cavity develops, and it collapses around $t = 44$ μs, approximately concurrently with the main cavitation bubble. Around 152 μs later ($t = 196.3$ μs), the slowed down particle is imaged at the upper central part of

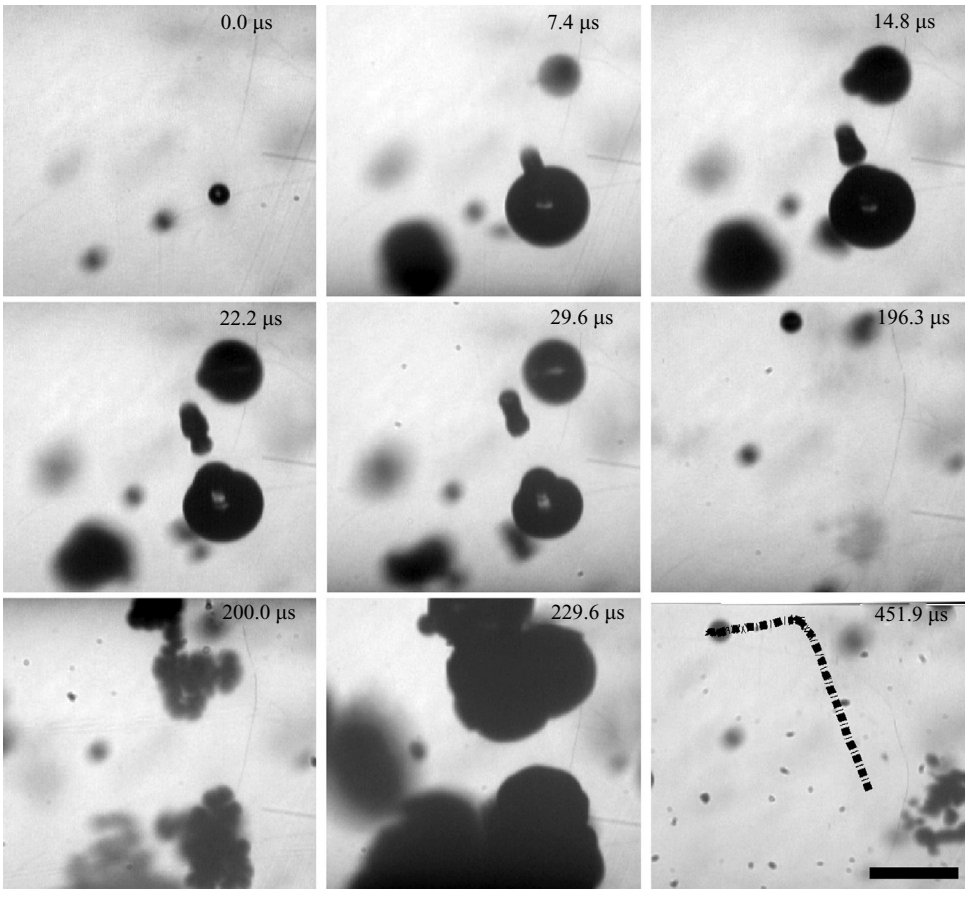

FIGURE 5. Experiment demonstrating that a particle being exposed twice to a shock wave can nucleate a cavitation bubble on its surface in both events. Here, a tensile stress wave excites cavitation at $t = 0$ and at $t = 200\,\mu s$. The trajectory of the particle is indicated in the last frame ($t = 451\,\mu s$) with the dashed black line. Note the different directions of motion induced at the successive cavitation events. The scale bar in the last frame is 500 μm in length. The lithotripter pulse motion is downwards in a direction 45° out of the photo-plane. Movie 2 is available with the online version of the paper.

the frame just prior to excitation with the second shock wave. At $t = 200\,\mu s$, a second cavitation bubble is in development on the particle and causes it to move, at this time to the left. This demonstrates that a particle can serve multiple times as a cavitation nucleus.

When at the first cavitation event the particle separates from the cavity and the neck gently closes, a cavitation nucleus may be left on its surface. Such a nucleus explains that in a number of cases a secondary attached cavity is observed to develop on the particle surface at low tensile stress, and it may form the site of inception when the next lithotripter pulse arrives, the direction of cavity growth being dependent on a possible particle rotation. However, even in the absence of such a nucleus, there may still be gaseous voids left on the particle surface which did not reach critical size when exposed to the first tensile pulse. The second pulse is weaker than the first as it is emitted from the back layer of the lithotripter, but the tensile stress field it sets up also depends on the cluster formation, and it may still be strong enough to cause a

second primary cavitation event from the same particle within the short time allowed between the pulses.

It should be noticed that the different directions of particle motion at exposure to successive waves emphasize that the motion is independent of the path of the acoustic wave, and is determined by the random position of nuclei on the particle. Further, we find that a stronger cavitation activity is set up by the second shock wave, e.g. the frame at $t = 229.6\,\mu s$ (figure 5) is to a large extent covered by bubbles. The large number of cavities in the bulk of the water at the top and bottom of the frame at $t = 200\,\mu s$ is most probably caused by gas nuclei produced at disintegration of the first cavitation bubbles at their collapse. During cavity expansion, more gas diffuses into the bubble than is transported back into the liquid during its collapse. Thereby, a cavity leaves one or more gaseous nuclei. We can estimate the amount of gas collected in a cavity during a lifetime of $\sim 40\,\mu s$ to be 1.1×10^{-12} g, assuming that the cavity reaches a maximum radius of 200 μm in air-saturated water. It is equivalent to a gas bubble of 6 μm equilibrium radius. For the derivation of the gas-uptake equation, see the Appendix of Arora, Junge & Ohl (2005). An air bubble of radius 6 μm dissolves within approximately 1.2 s in gas-saturated water; see for example Sapozhnikov *et al.* 2002, Epstein & Plesset 1950, or Eller & Flynn 1963. However, the cavitation bubble may fragment at collapse (Brennen 2002), which reduces the time of dissolution. From the frame at $t = 200\,\mu s$, we can coarsely estimate the number of visible fragments to be about 50, which have survived the time interval of 156 μs between the first cavity collapse and the arrival of the second tensile stress wave. During this time, only gas bubble nuclei of radius up to 0.15 μm go into solution, whereas the surviving nuclei have a mean volume corresponding to radii of about 1.7 μm. Thus, with the second wave, gas bubbles originally below the imaging resolution can be made visible.

4. Potential flow models

4.1. *Introduction and comparison of the two models*

The growth of a supercritical cavitation bubble on a planar wall is essentially hemispherical, and is modelled well by potential flow theory (Bremond *et al.* 2006*a*, *b*). The wall acts as a mirror and thus the situation is equivalent to that of a spherically symmetric cavity. During supercritical expansion, surface tension and compressibility of water, as well as viscous effects, can be ignored. Following the same philosophy, the flow field around a cavity expanding from a particle can be modelled as a potential flow. Within the first (crucial) microsecond after nucleation, the cavity has already developed beyond supercritical size, but it is still small compared to the size of the particle and it grows hemispherically. Later on, the cavity becomes much larger than the particle, and it approaches a spherical shape. Hence, with the cavity following spherical bubble dynamics, potential theory can be used throughout the whole growth process.

Based on the same potential flow principles, two models of increasing complexity will now be presented. Potential theory is described by Laplace's equation, $\nabla^2 \Phi = 0$, where Φ is the velocity potential. In Model 1, the initial cavity considered (the cavitation nucleus) is already larger than the critical cavity, and it is assumed to be a small spherical vapour void with its centre attached to the particle, such that it resembles a hemispherical cavity. At exposure to a tensile stress pulse, it expands radially from its location of nucleation, while remaining in contact with the particle (unless it grows to swallow it). As it grows beyond the size of the particle, it embraces it more or less. A semi-analytical expression of the particle motion is derived. Model 2

uses the axisymmetric formulation of the boundary-integral method and thus accounts for the strong deformation of the bubble observed in the experiments. For ease of calculation, the cavitation nucleus is here assumed to be a spherical cavity of radius as in Model 1, positioned in very close proximity to the particle surface. The basic equations that the two models have in common are given below. In both models the local pressure, $p(\boldsymbol{x}, t)$, can be calculated with the unsteady Bernoulli equation, i.e.

$$\rho \frac{\partial \Phi(\boldsymbol{x}, t)}{\partial t} + \tfrac{1}{2}\rho \, |\boldsymbol{u}(\boldsymbol{x}, t)|^2 + p(\boldsymbol{x}, t) = p_\infty(t). \tag{1}$$

Here, $\boldsymbol{u}$ is the local fluid velocity, $\boldsymbol{u} = \nabla\Phi$, $\boldsymbol{x}$ is the position vector, t is time, and ρ is the liquid density. The pressure on the right-hand side of (1), $p_\infty(t)$, is set up by the applied pressure pulse and is a function of time only, not of space. Owing to the very short time scales considered, the effect of gravity can be neglected in (1). At the end of this section, it is explained how $p_\infty(t)$ was extracted from the experimental data. In Model 2, (1) is used to calculate the pressure distribution on the wetted surface of the particle. The non-wetted part is subjected to the pressure inside the cavity, p_c, but as this pressure as well as the surface tension σ are significant only until just after the critical conditions for the equilibrium cavitation nucleus are exceeded (Hilgenfeldt *et al.* 1998), they are of no importance for the particle acceleration, and they are neglected, thus $p_c = 0$ and $\sigma = 0$. The force balance of the particle is obtained by integrating the pressure distribution on the particle surface, and by applying Newton's second law:

$$\boldsymbol{F} = \int_S p\boldsymbol{n}\mathrm{d}S = m_p \boldsymbol{a}_p, \tag{2}$$

where S is the surface of the particle, $\boldsymbol{a}_p$ its acceleration, and $m_p = 4\pi R_p^3 \rho_p/3$ its mass. Note that there is no need to account for the added mass, since this effect is automatically incorporated in the surface integral of (2) (see Lamb 1932, pp. 160). In (2), $\boldsymbol{n}$ represents the normal vector at the particle surface. The effect of viscous drag on the particle can be included by addition of an effective drag force to (2). During cavity growth, drag is assumed to be negligible as compared to the strong acceleration force, but for the particle motion after cavity–particle detachment it is important, and it is included, see § 4.4 for a detailed discussion.

Provided only a single cavity is nucleated, the problem can be considered as axisymmetric. The velocity $\boldsymbol{u}_p$ and position $\boldsymbol{x}_p$ of the particle follows from the acceleration $\boldsymbol{a}_p$ by integration. At the moment the cavity first appears, $\boldsymbol{x}_p$ and $\boldsymbol{u}_p$ are zero. We define this time as $t = 0$, and proceed stepwise by applying the changing far field pressure and the corresponding cavity governed velocity parameters to (1) to determine $p(x, t)$, which is used in Model 1 (the spherical bubble model, described in § 4.2) as well as in Model 2 (BEM, see § 4.3). Then we calculate the force on the particle and its acceleration from (2), and derive its velocity and displacement by integration. Note that in Gracewski, Miao & Dalecki (2005) comparable models are used to describe bubble–particle interaction. However, in their work, the particle is fixed and of comparable or larger size than the cavities.

At first, it seemed reasonable to use the pressure profile measured without particles, i.e. the profile depicted in figure 2, as $p_\infty(t)$. However, when doing so the maximum cavity radii obtained were much larger than those observed in the experiments. The explanation of this observation is that neighbouring cavities alter the local pressure around a cavity (see for example, Tanguay & Colonius 2003; Zijlstra & Ohl 2008). Unfortunately, the local pressure cannot be measured directly, as described in § 2.

How do we then obtain the pressure profile that leads to the cavity dynamics we observe experimentally? We obtain it from the observed dynamics of the cavity radius R_c(t), i.e. we employ the bubble as a local pressure sensor. Particle-generated cavities grow almost spherically in the half-space of liquid which does not include the particle, and the momentary radius of a given cavity is determined from this part of the cavity. Now we can estimate the far-field pressure $p_\infty(t)$ which the cavity has experienced from the Rayleigh–Plesset equation (Brennen 1995)

$$\frac{-p_\infty(t)+p_C}{\rho}=\frac{3}{2}\left[\frac{\mathrm{d}R_c}{\mathrm{d}t}\right]^2+R_c\frac{\mathrm{d}^2R_c}{\mathrm{d}t^2}. \tag{3}$$

The pressure p_c inside the explosively expanding cavity is essentially the vapour pressure, which is small compared to the magnitude of $p_\infty(t)$. Thus we again set $p_c=0$. A smooth representation of the bubble radii which is required for the temporal derivatives, is obtained by spline interpolation of the measured cavity radius–time traces. After differentiating them twice, the pressure $p_\infty(t)$ can be calculated from (3).

4.2. *Model 1: the spherical bubble model*

In Model 1, we start from an initial spherical cavitation nucleus of radius $R_{c,0}=1\,\mu$m, with its centre on the particle surface, and let it expand spherically, i.e. the distortion from sphericity observed in the experiments is neglected. The initial centre of the cavity is assumed to be stationary. This can be justified at least for the cavity expansion phase, in which its added mass increases rapidly. Thus, we assume a velocity potential as for a spherical cavity undergoing radial expansion

$$\Phi=-\frac{R_c^2}{r}\frac{\mathrm{d}R_c}{\mathrm{d}t}. \tag{4}$$

The radial velocity at position r from the cavity centre is given by

$$|\boldsymbol{u}|=\frac{R_c^2}{r^2}\frac{\mathrm{d}R_c}{\mathrm{d}t}. \tag{5}$$

Here, r is the radial distance measured from the stationary centre of the cavity. Using (1) and (3), the pressure $p_\infty(t)$ can be eliminated. Now the local pressure $p(r,t)$ anywhere in the liquid is expressed in terms of the cavity radius and its temporal derivatives by

$$\frac{p(r,t)}{\rho}=\left(2\left(\frac{\mathrm{d}R_c}{\mathrm{d}t}\right)^2+R_c\frac{\mathrm{d}^2R_c}{\mathrm{d}t^2}\right)\left(\left(\frac{R_c}{r}\right)-1\right)-\frac{1}{2}\left(\frac{\mathrm{d}R_c}{\mathrm{d}t}\right)^2\left(\left(\frac{R_c}{r}\right)^4-1\right). \tag{6}$$

In (6), the pressure becomes 0 when r approaches R_c, and $p_\infty(t)$ when r goes to infinity. To evaluate the force integral in (2), the pressure on the surface of the particle has to be described. The part of it covered by the cavity ($\psi<\theta$, see figure 6) is subjected to the pressure $p_c\approx 0$, while the pressure distribution acting on the remaining wetted particle surface area ($\theta<\psi<\pi$) is approximated by the pressure field of (6).

For calculations of the particle motion, the values of R_c and its derivatives are used, as obtained from the experimentally observed cavity radii after they are processed with the spline interpolation mentioned in § 4.1. Equations (2)–(6) for Model 1 are solved numerically to determine the particle motion. This scheme is followed until cavity collapse; thereafter the particle motion is supposed to be influenced only by viscous drag, see § 4.4.

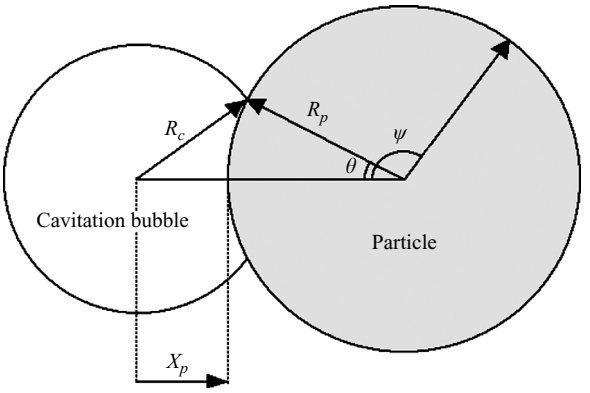

FIGURE 6. Sketch of the geometry for Model 1: a spherical cavitation bubble growing on a particle. The angle θ separates the non-wetted and wetted surface areas, and ψ identifies positions on the wetted surface. The coordinate of the particle displacement is X_p.

4.3. *Model 2: the axisymmetric boundary-element method (BEM)*

Model 2 is able to describe the deformation of the cavity during its expansion. The pressure p on the particle described by the unsteady Bernoulli equation, (1), is written for convenience in terms of the material derivative using $\boldsymbol{u}\cdot\nabla\Phi = \boldsymbol{u}\cdot\boldsymbol{u}$, thus

$$p(\boldsymbol{x}, t) = p_\infty(t) - \rho\frac{\mathrm{D}\Phi(\boldsymbol{x}, t)}{\mathrm{D}t} + \tfrac{1}{2}\rho|\boldsymbol{u}(\boldsymbol{x}, t)|^2. \tag{7}$$

This notation allows for a simpler implementation of the algorithm to obtain the potentials on the cavity surface from the previous time steps. The pressure $p_\infty(t)$ in (7) is calculated from the experimental cavity radius as mentioned in § 4.1. We note that although the bubble dynamics is modelled axisymmetrically, the driving pressure $p_\infty(t)$ is derived from a spherically expanding bubble model. The validity of this approach is outlined in the Appendix.

An elegant method for solving potential flow problems is the boundary-element method (BEM). It makes use of the fact that when either the potentials or their normal derivatives (the normal velocity in this case) are known on all boundaries of the problem at a given time, the whole flow field is determined. It has the further advantage that only boundary elements, here the moving particle and the growing cavity, need to be specified. Thus, there is no need to create a mesh for the whole fluid domain. For the problem under consideration, the following BEM-equation (see for example, Blake & Gibson 1987) is used:

$$c(\boldsymbol{x}_0)\Phi(\boldsymbol{x}_0) + \int_{S+C}\Phi(\boldsymbol{x})\frac{\partial G(\boldsymbol{x}_0, \boldsymbol{x})}{\partial n}\,\mathrm{d}S = \int_{S+C}G(\boldsymbol{x}_0, \boldsymbol{x})\frac{\partial\Phi(\boldsymbol{x})}{\partial n}\,\mathrm{d}S. \tag{8}$$

Here, $\boldsymbol{x}_0$ points to a node describing either the cavity or the particle surface. The variable $c(\boldsymbol{x}_0)$ is the solid angle, G is the Green function, and $\partial/\partial n = \boldsymbol{n}\cdot\nabla$. The integration in (8) must be done on both objects, the cavity surface 'C' and the particle surface 'S'. At every new time step, the potential is updated on the cavity surface 'C' with the rephrased Bernoulli equation (1)

$$\rho\frac{\mathrm{D}\Phi}{\mathrm{D}t} = \tfrac{1}{2}\rho|\boldsymbol{u}|^2 + p_\infty(t). \tag{9}$$

Again, we assume the pressure inside the cavity to be $p_c = 0$, see § 4.2. The normal derivative of the potential, i.e. the normal velocity, on the particle is obtained through:

$$\frac{\partial \Phi}{\partial n} = \boldsymbol{n} \cdot \boldsymbol{u}_p. \tag{10}$$

Still the potential on the particle surface and the normal velocity on the cavity have to be determined. The numerical scheme divides the cavity and particle surfaces into linear elements connected by nodes (51 nodes on the cavity and 51 nodes on the particle). The nodes are distributed equidistantly on the surface of the bubble and the particle. Following the standard procedure in BEM (8) is rewritten into a matrix equation relating the potential and its normal derivative at each node to all other ones (see Harris 1993 for more details). The matrix equation is solved for $\partial \Phi / \partial n$ on the cavity and Φ on the particle. This method is described in more detail in Wang *et al.* (1996), Rungsiyaphornrat *et al.* (2003) and Khoo, Klaseboer & Hung (2005).

With (7), the pressure on the surface of the particle can be calculated, while (2) gives the force. The velocity and the position of the particle are then obtained by integration. Finally, the cavity surface position is obtained from $\partial \Phi / \partial n$. In order to prevent unphysical behaviour and numerical instabilities, the minimum distance between the cavity-nodes and the particle-nodes is limited to the inter-node distance on the particle surface. When this happens, the pressure on the particle is set to $p = p_c = 0$ for the evaluation of the force with (2).

The initial cavity is taken to be a full sphere of radius $R_{c,0} = 1\,\mu\text{m}$ (corresponding roughly to the inter-node distance on the particle). The sensitivity to the choice of $R_{c,0}$ has been tested and even a value of $R_{c,0} = 10\,\mu\text{m}$ gives results that differ by less than a few per cent. In the calculations, we use the initial expansion rate $\mathrm{d}R_c/dt = 0$ and $p_\infty(t) = 0$. Although these initial conditions are a simplified version of the physics involved, they do not influence the numerical results for the experimental conditions, see § 5.1.

4.4. *Viscous effects*

The drag force has been neglected during the first stages of particle acceleration because the pressure force acting on the particle is much larger. However, as the particle moves away from the bubble, viscous forces slow down the particle and eventually it comes at rest. Usually, viscous effects are taken into account by introducing the drag force and the Basset history force (Clift, Grace & Weber 1978). The latter is neglected for simplicity. The former is written as:

$$\boldsymbol{F}_d = \tfrac{1}{2}\rho\pi R_p^2 C_d(Re)|\boldsymbol{u}_p - \boldsymbol{u}|(\boldsymbol{u}_p - \boldsymbol{u}), \tag{11}$$

where $C_d(Re)$ is the Reynolds number dependent drag coefficient. The Reynolds number is based on the particle diameter and the relative velocity, $\boldsymbol{u}_p - \boldsymbol{u}$. The drag coefficient C_d is approximated (Clift *et al.* 1978) by the following expressions

$$C_d = \frac{24}{Re}(1 + 0.15 \times Re^{0.687}), \quad 200 < Re < 800, \tag{12a}$$

$$C_d = 0.44, \quad Re > 800. \tag{12b}$$

After the particle has been ejected from the bubble, the Reynolds number reaches values of 2000 to 5000 for the three cases studied in §§ 5.2 to 5.4. To account for viscous drag after the detachment of the particle from the cavity surface, (2) is replaced by

$$\boldsymbol{F} = \int_S p\boldsymbol{n}\,\mathrm{d}S - \boldsymbol{F}_d = m_p \boldsymbol{a}_p. \tag{13}$$

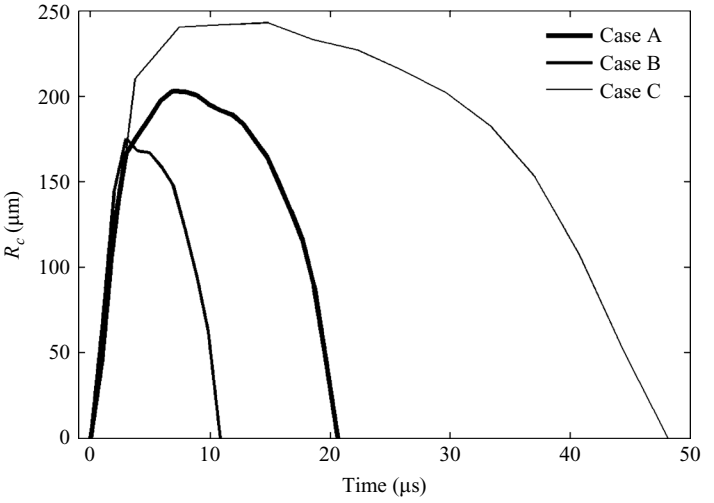

FIGURE 7. Experimentally determined cavity radii as a function of time for Cases A, B and C. Here, Case A corresponds to a particle of $R_p = 68\,\mu\text{m}$ and maximum cavity radius $R_c^{max} = 203\,\mu\text{m}$, Case B to $R_p = 30\,\mu\text{m}$ and $R_c^{max} = 175\,\mu\text{m}$, and Case C to $R_p = 62\,\mu\text{m}$ and $R_c^{max} = 243\,\mu\text{m}$.

5. Comparison of experiments with simulations

5.1. *Preliminary remarks*

We have compared the observed particle motion in three cavitation experiments with simulated particle motions based on the two models presented above. As explained in § 4.1, the pressure that drives the cavity dynamics and the particle motion can be evaluated only from the experimental radius *vs.* time curve of the cavity, because more direct local pressure measurements are not possible, and thus the evaluation of $p_\infty(t)$ is based on the idealized conditions of the Rayleigh–Plesset equation. The three measured cavity radii (the cavity remains almost spherical outside the region with the particle) are shown in figure 7. The last frame without a visible cavity is used as the starting point $t = 0$ for the simulations of $p_\infty(t)$, and the initial position of the point on the particle surface from which the cavity develops is taken as $x_p = 0$, see figure 6. The pressure profiles $p_\infty(t)$ calculated from the $R_c(t)$ curves are shown in figure 8.

We notice that all cases show $\mathrm{d}p/\mathrm{d}t = 0$ at $t = 0$, which misrepresents what actually happens during the inception period. However, it is a consequence of the initial boundary conditions for the spline interpolation which are chosen to be $\mathrm{d}R/\mathrm{d}t = 0$ at $t = 0$, because the cavity is initially at rest, and $R(t = 0) = R_0$.

Furthermore, we remark that the observed pressure profiles are very different from each other, and we ascribe this to differences between the cavity clusters generated in the individual experiments. We also notice that in the Cases A and B, the calculated maximum tensile stress is notably higher than that measured for a lithotripter pulse without cavitation. In this context, it should be noted that owing to the assumption of incompressible flow, the maximum tensile stress, calculated from (1), is overestimated, see also the discussion on compressibility effects in bubbly clouds in Hamilton *et al.* (2005). However, during the fast initial cavity growth which is decisive for the particle acceleration, only a small volume of liquid relaxes, and therefore the assumption of incompressibility is acceptable.

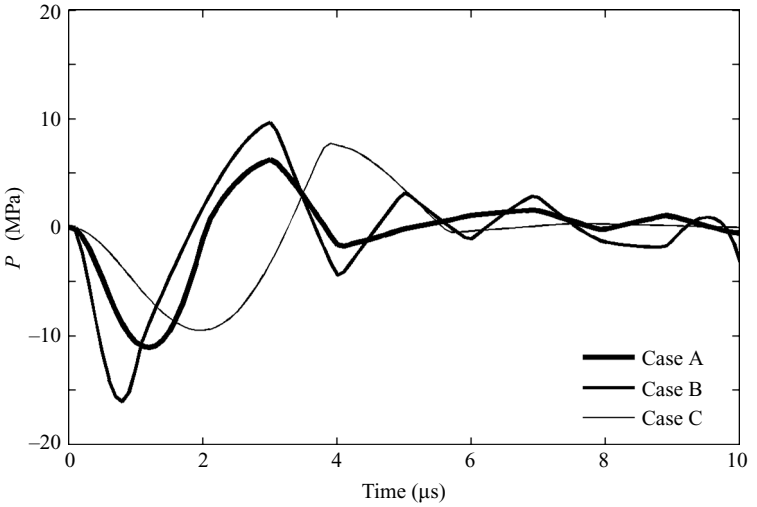

FIGURE 8. Calculated pressures $p_\infty(t)$ deduced from the experimental cavity radii as shown in figure 7 for Cases A, B and C.

With the BEM model, the simulations are stopped just before the final stage of cavity collapse. To reflect the slowing down of the particle motion owing to the drag force, the simulations with the spherical cavity model are continued beyond the cavity collapse.

In previous experiments (Arora *et al.* 2004) we found that cavitation inception occurs in the focal region once the tensile stress exceeds a certain limit. Actually, a value of $p_\infty(t) < -2.5$ MPa (corresponding to a critical cavity radius of $\sim$50 nm) was necessary to initiate cavitation. However, we do not know the critical stress for each individual cavitation event observed in the current photographic series. Inception occurs within one frame interval, i.e. between the last picture without a cavity and the first one with a visible cavity. The use of $p_\infty(t=0)=0$ as the cavitation threshold introduces an error, but it is small because it takes only about 200 ns for the pressure to drop from a slightly positive pressure level to one below -2.5 MPa (see figure 2), and the frame intervals are at least $\sim$1 μs. By varying $p_\infty(t=0)$ between 0 and -5 MPa we found a negligible effect on the particle trajectory, demonstrating the robustness of the approach.

5.2. *Case A: particle radius 68 μm, maximum cavity radius 203 μm*

Case A, shown in figure 3 (and discussed in § 3), depicts cavitation on a polystyrene particle of radius $R_p = 68$ μm recorded at a framing rate of 1.02 million frames s^{-1}. The initial growth of the cavity radius R_c is very rapid, reaching 120 μm in only 2 μs (Case A, figure 7). The framing rate is sufficient to give a reliable growth rate. The cavity acquires its maximum size $R_c^{max} = 203$ μm in 7.8 μs, then it starts collapsing, but less violently than the initial growth. The pressure profile used for calculations with both models is given in figure 8. The maximum negative pressure is about -11 MPa, i.e. notably lower than the value of -7 MPa measured in water without particles (figure 2), as discussed before (§ 5.1). Subsequently, the pressure rises steeply and becomes positive again at $t = 2.0$ μs, i.e. notably earlier than the pressure measured in the absence of particles, see figure 2. It reaches a maximum positive value of $\sim$6 MPa before it drops, oscillating towards 0.1 MPa.

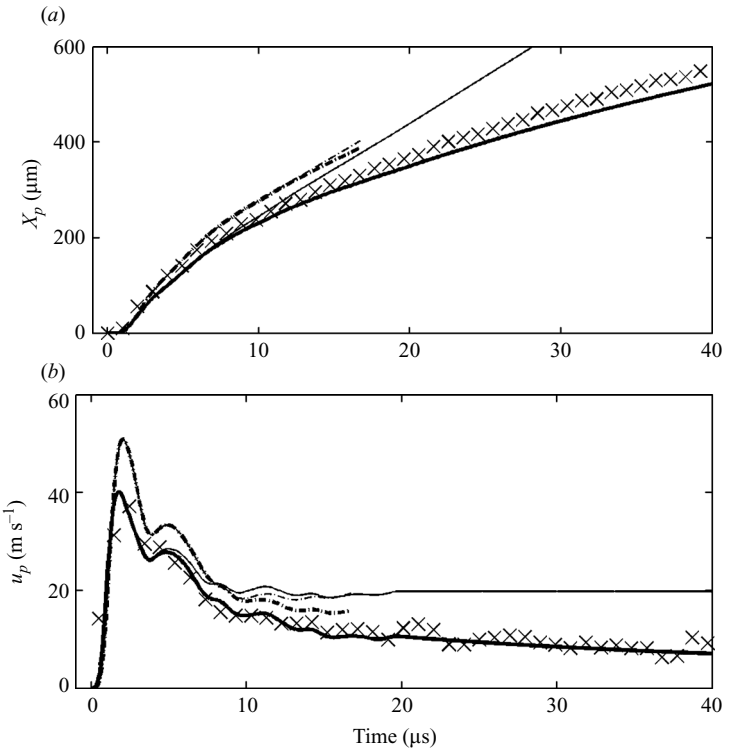

FIGURE 9. Comparison of the experimental Case A, $R_p = 68\,\mu\text{m}$ with simulations from both models. The particle positions are compared in (*a*) and the velocities of the particle in (*b*). The experimentally determined values are indicated with crosses, while the lines are the results from the models. The spherical bubble model (Model 1) simulations are drawn as solid lines and the axisymmetric BEM simulations (Model 2) are drawn with dashed-dotted lines. Computational results including viscous friction (from the moment of detachment) are drawn with thick lines, and those neglecting viscosity with thin lines.

In figure 9 the particle position and velocity *vs.* time curves found experimentally are shown together with those simulated with Models 1 and 2. It is apparent that viscous effects are important when the particle has detached from the cavity, and the agreement between experiment and simulation when these effects are included shows that the above calculation of the drag is adequate. Also, the linear position *vs.* time relationships obtained in the simulations without the viscous effects after detachment demonstrate that the cavity dynamics ceases to influence the motion of the particle. The S-shape of the particle displacement *vs.* time curve is a result of positive acceleration of the particle during the period of tensile stress in the liquid and negative acceleration when the pressure rises and becomes positive for $t > 2\,\mu\text{s}$. During positive particle acceleration, the cavity grows from a small size, and the drop of pressure across the particle is very high. Therefore the particle acquires a high kinetic energy. During the subsequent negative acceleration, the cavity is large and the adverse pressure drop is smaller, which allows the particle to retain a considerable kinetic energy. Thus, at particle detachment the particle velocity u_p has the value of $\sim 14\,\text{m s}^{-1}$. Model 1 predicts a maximum velocity of $\sim 40\,\text{m s}^{-1}$, which agrees well with the experimental observations. Thus, the spherical cavity model captures the main features of the experimentally observed particle motion driven by the initial rapid growth of the cavitation bubble. However, the changes of the cavity shape are

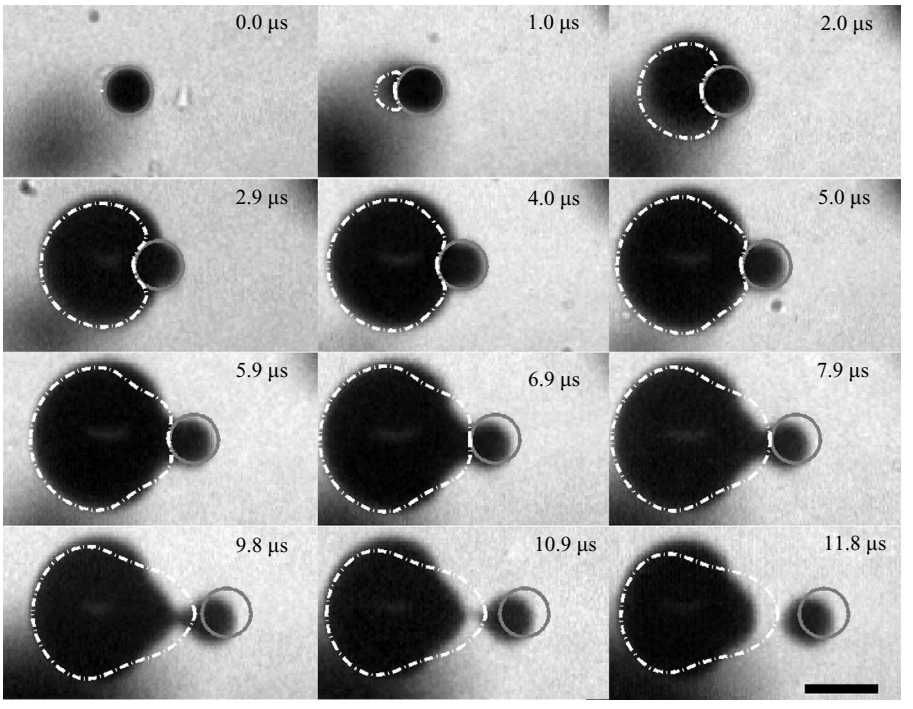

FIGURE 10. The cavity shapes (dash-dotted curves) and particle positions (grey solid lines) obtained by BEM calculations compared with the corresponding high-speed recordings (Case A). The cavity is taken to be nucleated at $t = 0\,\mu s$. At $t = 2.9\,\mu s$, the cavity partly wraps the particle, and at $t = 7.8\,\mu s$, a neck is created. Good agreement between the BEM calculations and the experiment is found until $t = 5.9\,\mu s$. After this time, and in particular after detachment of the particle from the cavity at $t = 10.8\,\mu s$, clear deviations are found in the cavity shape; presumably because the attachment of the cavity to the particle surface is not modelled in the BEM calculations. The scale bar shown is 200 μm.

not accounted for by this simple model. For this, the boundary-element method is required.

In the BEM simulation (Model 2), the spherical cavitation nucleus is subjected to the same pressure profile as used for Model 1 (Case A of figure 8). With (2), the force acting on the particle is calculated, and by integration, its velocity and position are found. In figure 10, the calculated cavity shapes and particle positions are plotted on top of selected frames from the experiment (figure 3). The outlines of the particle and the cavity obtained from the simulations are depicted with a solid grey and a white dashed line, respectively. At $t = 0\,\mu s$, cavitation inception is indicated by a small dot immediately to the left of the particle. Subsequently, the cavity starts growing and partly wraps the particle from $t = 1.0\,\mu s$ to $t = 5.9\,\mu s$. At the same time, the particle is accelerated away from the cavity. On the particle surface in contact with the cavity the pressure is close to 0, while on the opposite side it is still strongly negative. We find good agreement between the experiment and the BEM calculated cavity shape and the positions of the cavity and particle until the neck formation is initiated, starting for $t > 5.9\,\mu s$ in figure 10. In the experiment the right-hand cavity surface, which is attached to the particle, is stretched and elongates into a thin neck at $t = 9.8\,\mu s$, until detachment from the particle. The BEM simulations do not reveal this cavity dynamics, because the liquid–gas–particle contact condition

is omitted, see §4.3. Thus, it is not surprising that differences in the cavity shape between simulation and experiment occur from shortly before the necking and during the collapse of the neck, i.e. in the time interval from $t = 5.9\,\mu s$ to $11.8\,\mu s$. However, the basic cavity deformation during growth, related to the cavity–particle interaction is well reproduced in the simulation.

From this time, the particle moves away from the cavity at slowly decreasing speed. The neck-breaking initiates a surface wave on the cavity, which results in the typical 'mushroom' shape observed in figure 3, e.g. at $t = 14.7\,\mu s$. In the experiment, the cavity collapses at $\sim 20.6\,\mu s$, but at this time the particle is already relatively far from the cavity which does not seem to influence the particle motion any more.

When the particle starts to move away from the cavity, the radial velocity and the pressure gradient in the liquid are small, but the particle motion through the liquid causes a loss of kinetic energy by friction. An additional source of energy loss is the creation of the neck. In general, the surface energy $E_n = 2\pi r_n \sigma l_n$, where r_n is the neck radius, σ the coefficient of surface tension, and l_n the length of the neck, is negligible for the particle sizes considered in this study. However, for smaller particles, the surface energy can become comparable with the kinetic energy. For particles below $\sim 100\,nm$, all of the kinetic energy will be required in order to create the surface, assuming $l_n = R_p$, $r_n = R_p$, $\sigma = 0.06\,N\,m^{-1}$, and $u_p = 40\,m\,s^{-1}$.

5.3. *Case B: particle radius 30 μm, maximum cavity radius 175 μm*

Another case of polystyrene particle acceleration is depicted in figure 11. The motion of the particle of $R_p = 30\,\mu m$ is visible in each frame, and a cavity develops (figure 7, Case B), reaching a maximum radius of $R_c^{max} = 175\,\mu m$, owing to the tensile stress in its far field. As in Case A, a framing rate of 1.02 million frames s^{-1} was used, i.e. sufficient to give a reliable initial cavity growth rate and pressure profile (figure 8, Case B). Experimentally, the cavity collapses $10.8\,\mu s$ after it has been created. Thus, the collapse time is much shorter than in Case A because the trailing positive pressure pulse arrives earlier and it is stronger. We notice that in the simulation with Model 1, the particle becomes engulfed by the cavity in the time interval from $t = 1\,\mu s$ to $t = 3\,\mu s$, which leads to a zero force and thus to a constant particle velocity in this interval of time. This does not occur for Model 2. Consequently, the maximum velocities calculated from the two models differ substantially. The BEM model apparently overestimates the displacement of the particle, even when viscous drag is included. However, the increase of the particle blurriness recorded experimentally suggests that an out-of-plane motion of the particle occurred. This indicates that the particle velocity is higher than the one we calculate assuming in-plane motion.

5.4. *Case C: particle radius 62 μm, maximum cavity radius 243 μm*

Figure 12 shows the dynamics of a particle of radius $62\,\mu m$ set up during the growth of a cavity to a maximum radius of $R_c^{max} = 243\,\mu m$ and with a lifetime of $48\,\mu s$ (figure 7, Case C), recorded at a framing rate of 0.27 million frames s^{-1}. The calculated pressure profile is shown in figure 8. Until inception, we can assume that the pressure pulses are reproducible and well represented by figure 2, but after inception the pressure depends on the development of the cavity cluster, and the rate of change of the pressure varies from experiment to experiment. However, the dynamics of the particle motion is well simulated by both models, when the effect of viscous drag is taken into consideration.

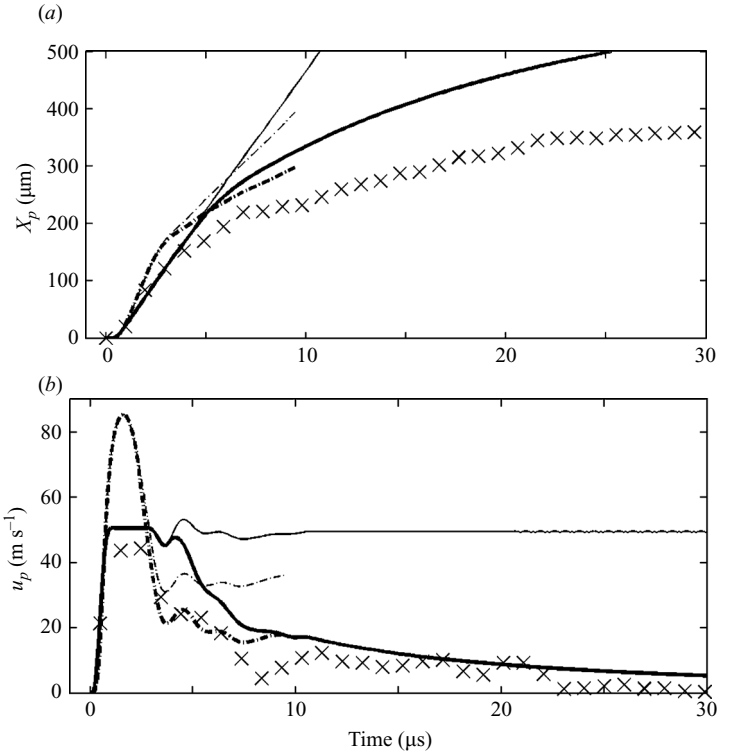

FIGURE 11. Comparison of the experimental Case B, $R_p = 30\,\mu\text{m}$ with simulations from both models. The particle positions are compared in (*a*) and the velocities of the particle in (*b*). The experimentally determined values are indicated with crosses, while the lines are the results from the models. The spherical bubble model (Model 1) simulations are drawn as solid lines and the axisymmetric BEM simulations (Model 2) with dashed-dotted lines. Computational results including viscous friction are drawn with thick lines, and those neglecting viscosity with thin lines.

6. Injection into elastic material

The very strong particle acceleration due to the explosive cavity expansion suggests that it might be possible to inject particles into a bulk elastic material by this technique. To achieve entrainment of particles into a material, the threshold strain of its elastic–plastic transition has to be overcome. We choose gelatin (3 % vol. concentration) as the receiving bulk material together with the polystyrene particles. For the experiment, a microscope slide is covered with a layer of gelatin, approximately 2 mm thick and submerged in water with suspended particles. The cavity and particle dynamics are recorded with a set-up similar to that depicted in figure 1; only a different high-speed framing camera is used (Photron APX, Photron Ltd, Marlow, Bucks, UK). An experiment showing implantation of a particle into gelatin is depicted in figure 13. In the first frame the geometry is sketched: water at the left hand side and gelatine at the right hand side. The frames in this figure are selected from a high-speed series taken at 125 000 frame s^{-1}. The time of recording is given relative to the moment of cavitation inception. A particle adhering to the water/gelatin interface is depicted in figure 13, $t = -10\,\mu\text{s}$. A cavity has formed 8 μs after inception on the surface of the particle, and it develops in the water environment only. The particle detaches from this cavity between the frames at 8 μs and at 26 μs and propels towards the right into

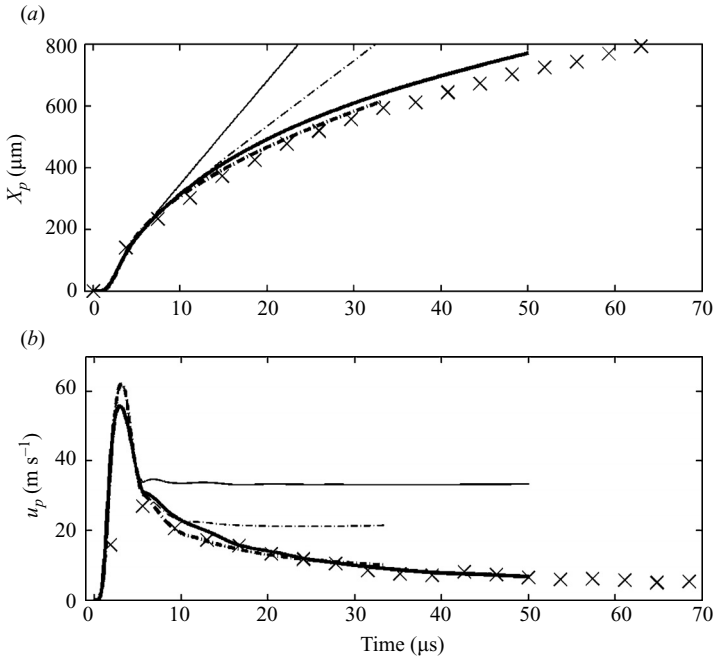

FIGURE 12. Comparison of the experimental Case C, $R_p = 62\,\mu\text{m}$ with simulations from both models. The particle positions are compared in (*a*) and the velocities of the particle in (*b*). The experimentally determined values are indicated with crosses, while the lines are the results from the models. The spherical bubble model (Model 1) simulations are drawn as solid lines and the axisymmetric BEM (Model 2) simulations with dashed-dotted lines. Computational results including viscous friction are drawn with thick lines, and those neglecting viscosity with thin lines.

the gelatin (particle 1 in figure 13, 26 μs). Particle 2 is shot into the gelatin close to particle 1 from another cavity not visible in the recorded section, but located in the bulk phase of the fluid below to the left. The visible cavity collapses between 53 μs and 97 μs (figure 13). Particle 1 continues to penetrate deeper into the material (∼350 μm) whereas particle 2 resides around 100 μm below the water–gelatin interface. Later, particle 1 is slightly pushed back, but remains inside the gelatin; in contrast, particle 2 is ejected back into the liquid, see $t = 373\,\mu\text{s}$, figure 13.

The reason for the difference in penetration is presumably the difference of the momentum of the particles. Not only is particle 1 larger, it is also accelerated directly from the interface, whereas particle 2 travels through water before it hits the interface, and therefore presumably has a slower impact velocity.

This experiment demonstrates that particles close to an elastic interface can be implanted in the substance by cavitation activity. Thus also particles containing drugs may be delivered from a liquid environment into tissue by non-invasive means. The method is also able to target a certain site within tissue by using a focused wave, a technique already used in kidney stone fragmentation (lithotripsy). Another medical application could be transdermal delivery of pharmaceuticals. Here, the particles serving as drug vehicles are brought on top of the skin and become exposed to the tensile wave through a coupling medium.

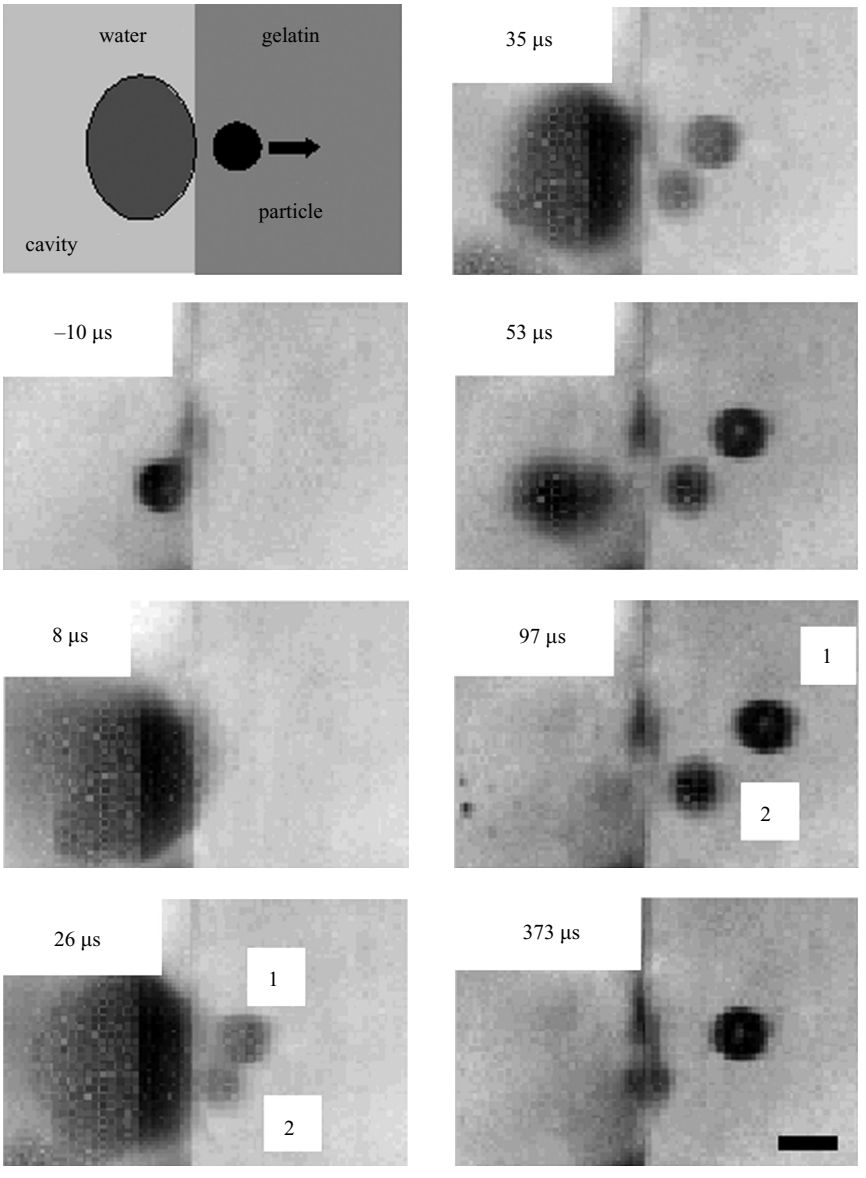

FIGURE 13. Particle injection into gelatin induced by cavitation. The first picture shows the fluid environment. The water–gelatin interface is located along the vertical centreline of the frame. At $t = \sim 10\,\mu s$, a particle of radius $\sim 50\,\mu m$ is initially located in the water, touching the gelatin. This particle (denoted 1 in the frames taken at $t = 26\,\mu s$ and $t = 97\,\mu s$) holds a cavitation nucleus that explodes, and the particle is shot into the gelatin. The process is shown in the subsequent frames. A second particle (denoted 2, radius about $40\,\mu m$) is accelerated from some distance and under an angle from below. It penetrates into the gelatin shortly before $t = 26\,\mu s$. Particle 1 stays entrained after the cavitation activity has ceased ($t = 373\,\mu s$) whereas particle 2 is repelled from the elastic material. The maximum radius of the cavity propelling particle 1 is almost $200\,\mu m$. The scale bar in the last frame is $100\,\mu m$ in length. Movie 3 is available with the online version of the paper.

7. Conclusions

Cavitation bubbles expanding from suspended particles cause rapid particle acceleration. The pressure difference across the particle during the expansion of the cavity results in a net force that accelerates the particle. When the cavity reaches its maximum size, part of it remains attached to the particle for some time ('necking'). When the cavity finally collapses, the particle is already quite far away and the final cavity dynamics has little influence on the dynamics of the particle. The results show that the spherical cavity model (Model 1) and the BEM simulations (Model 2) are both consistent with the experimental data obtained. The cavity shapes calculated by the axisymmetric BEM agree well with the experiments until neck formation sets in. At later times, the calculated cavity shapes differ from the experimental ones presumably owing to the neglect of the cavity–particle contact condition in these simulations.

Further studies are required to show how the particle velocities depend on applied pressure (i.e. maximum bubble size), particle diameter, particle density, particle shape, etc.

The feasibility of cavitation-induced particle implantation in a gelatine phantom has been demonstrated which might open up a new working principle to implant particles into tissue, e.g. for drug delivery. We could think of biodegradable particles serving as drug containers carrying cavitation nuclei which allow them to be implanted into cells. This method, when used with a focused extracorporeal acoustic source, would have the additional advantage of being local (order of 1 cm in width, and 10–15 cm in depth). Another potential lies in particle penetration through skin for transdermal drug delivery or vaccination.

We acknowledge financial support from NWO (C. D. O, VIDI grant), STW (B. B., NanoNed programme), and FOM (M. A., Physics for Medical Technology program). C. D. O. thanks IHPC (Singapore) for hosting him in January 2007.

Appendix. Is $p_\infty(t)$ suited for the description of the non-spherical cavity dynamics?

Equation (3) for the pressure $p_\infty(t)$ is derived under the assumption of purely radial symmetry (isotropy). However, the BEM model uses an axisymmetric formulation. In this Appendix, we discuss the validity of this approximation. The reference pressure $p_\infty(t)$ used in the numerical simulations is calculated from the experimental cavity radius (see §4.1). Clearly, far away from the bubble, isotropy is given, but it breaks down close to the bubble. At large distances, only the first-order source/sink terms are important; any higher-order terms, such as dipoles, will approach zero much more quickly. The true motion of the cavity will not of course be spherically symmetric, as part of the cavity surface is bounded by the particle.

In order to check how well the assumption of the far-field pressure $p_\infty(t)$ in (1) works for describing the non-spherical dynamics, we compare in figure 14 the radial dynamics from the Case A experiment (interpolated to splines for a smooth representation, see §4.1) with a volume-averaged radius extracted from the BEM (Model 2). Indeed, in the first few microseconds, some differences occur which we attribute to the particle–cavity interaction being predominant, until the cavity grows to a size larger than the particle. Thereafter, the pressure function $p_\infty(t)$ leads to a good calculation of the experimental cavity radius until collapse of the cavity. Figure 14(*b*) reveals that the relative deviation between the radius obtained in the BEM simulation

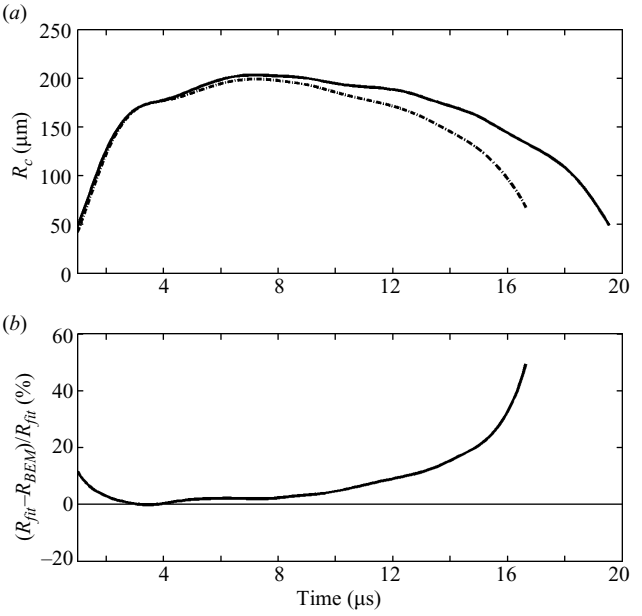

FIGURE 14. (*a*) The smooth representation of the cavity radius $R_c(t)$ from the experiment (solid line) is compared with the volume averaged radius from the BEM (dashed dotted line). (*b*) The relative deviation of these two curves is given in percent.

and in the experiment is below 10 % most of the time, but it increases to 50 % during the collapse phase.

Another cause of the difference might lie in the limited number of experimental data points available during the initial bubble expansion. Here, small differences in the smooth representation between two measured radii caused by the fitting procedure can introduce a substantial error because a second temporal derivative of the cavity radius has to be employed in order to calculate $p_\infty(t)$.

Finally we want to emphasize that on the time scales of the pressure recordings, the far-field pressure obtained through (3) does not display rapid local pressure changes which are probably present and generated from nearby collapsing bubbles (see Zijlstra & Ohl 2008). However, it can be concluded from Klaseboer *et al.* (2006, 2007) that these pressure pulses are not very intense, otherwise we would have observed jets in random directions.

REFERENCES

APFEL, R. E. 1970 The role of impurities in cavitation-threshold determination. *J. Acoust. Soc. Am.* **48**, 1179–1186.

ARORA, M., OHL, C. D. & MØRCH, K. A. 2004 Cavitation inception on microparticles: a self-propelled particle accelerator. *Phys. Rev. Lett.* **92**, 174501.

ARORA, M., JUNGE, L. & OHL, C. D. 2005 Cavitation cluster dynamics in shock-wave lithotripsy: Part 1. Free field. *Ultrasound Med. Biol.* **31**, 827–839.

ARORA, M., OHL, C. D. & LOHSE, D. 2007 Effect of nuclei concentration on cavitation cluster dynamics. *J. Acoust. Soc. Am.* **121**, 3432–3436.

ATCHLEY, A. & PROSPERETTI, A. 1989 The crevice model of bubble nucleation. *J. Acoust. Soc. Am.* **86**, 1065–1084.

Blake, J. R. & Gibson, D. C. 1987 Cavitation bubbles near boundaries. *Annu. Rev. Fluid Mech.* **19**, 99–123.

Borkent, B. M., Arora, M. & Ohl, C. D. 2007 Reproducible cavitation activity in water–particle suspensions. *J. Acoust. Soc. Am.* **121**, 1406–1412.

Bremond, N., Arora, M., Ohl, C. D. & Lohse, D. 2005 Cavitation on surfaces. *J. Phys. Condensed Matter* **17**, S3603–S3608.

Bremond, N., Arora, M., Ohl, C. D. & Lohse, D. 2006*a* Controlled multibubble surface cavitation. *Phys. Rev. Lett.* **96**, 224501.

Bremond, N., Arora, M., Dammer, S. M. & Lohse, D. 2006*b* Interaction of cavitation bubbles on a wall. *Phys. Fluids* **18**, 121505.

Brennen, C. E. 1995 Cavitation and bubble dynamics. Oxford University Press.

Brennen, C. E. 2002 Fission of collapsing cavitation bubbles. *J. Fluid Mech.* **472**, 153–166.

Chin, C. T., Lancée, C., Borsboom, J., Mastik, F., Frijink, M. E., de Jong, N., Versluis, M. & Lohse, D. 2003 Brandaris 128: A digital 25 million frames per second camera with 128 highly sensitive frames. *Rev. Sci. Instrum.* **74**, 5026–5034.

Clift, R., Grace, J. R. & Weber, M. E. 1978 *Bubbles, Drops and Particles.* Academic.

Crum, L. A. 1979 Tensile strength of water, *Nature* **278**, 148–149.

Eller, A. & Flynn, H. G. 1963 Rectified diffusion during nonlinear pulsations of cavitation bubbles. *J. Acoust. Soc. Am.* **37**, 493–503.

Epstein, P. S. & Plesset, M. S. 1950 On the stability of gas bubbles in liquid/gas solutions. *J. Chem. Phys.* **18**, 1505–1509.

Gracewski, S. M., Miao, H. & Dalecki, D. 2005 Ultrasonic excitation of a bubble near a rigid or deformable sphere: implications for ultrasonically induced hemolysis. *J. Acoust. Soc. Am.* **117**, 1440–1447.

Green, J. L., Durben, D. J., Wolf, G. H. & Angell, C. A. 1990 Water and solutions at negative pressure: Raman spectroscopy study to −80 megapascals. *Science* **249**, 649–652.

Greenspan, M. & Tschiegg, C. E. 1967 Radiation induced acoustic cavitation; apparatus and some results. *J. Res. Natl Bur. Stand. C Engng Instrum.* **71C**, 299–312.

Hamilton, M. F., Ilinskii, Y. A., Douglas Meegan, G. & Zabolotskaya, E. A. 2005 Interaction of bubbles in a cluster near a rigid surface. *Acoust. Res. Lett. Online* **6**, 207–213.

Harris, P. J., 1993 A numerical method for predicting the motion of a bubble close to a moving rigid structure. *Commun. Numer. Meth. Engng* **9**, 81–86.

Harvey, E. N., Barnes, D. K., McElroy, W. D. Whiteley, A. H., Pease, D. C. & Cooper, K. W. 1944 Bubble formation in animals. *J. Cell Comput. Physiol.* **24**, 1–22.

Hilgenfeldt, S., Brenner, M. P., Grossmann, S. & Lohse, D. 1998 Analysis of Rayleigh–Plesset dynamics for sonoluminescing bubbles. *J. Fluid Mech.* **365**, 171–204.

Holmberg, M., Kühle, A., Garnæs, J., Boisen, A. & Mørch, K. A. 2003 Cavitation nuclei at water–gold interfaces. *Fifth Intl Symp. Cavitation, Osaka, Japan, November 1–4, 2003.*

Khoo, B. C., Klaseboer, E. & Hung, K. C. 2005 A collapsing bubble-induced micro-pump using the jetting effect. *Sensors Actuators* A **118**, 152–161.

Klaseboer, E., Turangan, C., Fong, S. W., Liu, T. G., Hung, K. C., Khoo, B. C. 2006 Simulations of pressure pulse–bubble interaction using boundary element method. *Comput. Meth. Appl. Engng* **195**, 4287–4302.

Klaseboer E., Fong, S. W., Turangan, C. K., Khoo, B. C, Szeri, A. J. Calvisi, A. J., Sankin, G. N. & Zhong, P. 2007 Interaction of lithotripter shockwaves with single inertial cavitation bubbles. *J. Fluid Mech.* **593**, 33–56.

Lal, M. K. & Menon, S. 1996 Interaction of two underwater explosion bubbles. *ASME Fluids Engng Div. Conf.* **236**, 595–600.

Lamb, H. 1932 *Hydrodynamics,* 6th edn. Cambridge University Press.

Liebler, M. Dreyer, T. & Riedlinger, R. E. 2006 Nonlinear modelling of interactions between ultrasound propagation and cavitation bubbles. *Acta Acust.* **92**, 165–167.

Madadnia, J. & Owen, I. 1993 Accelerated surface erosion by cavitating particulate-laden flows. *Wear* **165**, 113–116.

Madadnia, J. & Owen, I. 1995 Erosion in conical diffusers in particulate-laden cavitating flow. *Intl J. Multiphase Flow* **21**, 1253–1257.

Madanshetty, S. I. 1995 A conceptual model for acoustic microcavitation. *J. Acoust. Soc. Am.* **98**, 2681–2689.

Marschall, H., Mørch, K. A., Keller, A. P. & Kjeldsen, M. 2003 Cavitation inception by almost spherical solid particles in water. *Phys. Fluids* **15**, 545–553.

Mørch, K. A. 2000 Cavitation nuclei and bubble formation – a dynamic liquid–solid interface problem. *Trans. ASME* I: *J. Fluids Engng* **122**, 494–498.

Mørch, K. A., 2007 Reflections on cavitation nuclei in water. *Phys. Fluids*, **19**, 072104.

Pishchalnikov, Y. A., Sapozhnikov O. A., Bailey M. R., Pishchalnikova I. V., Williams J. C. & McAteer J. A. 2005 Cavitation selectively reduces the negative-pressure phase of lithotripter shock pulses. *Acoust. Res. Lett. Online* **6**, 280–286.

Rungsiyaphornrat, S., Klaseboer, E., Khoo, B. C. & Yeo, K. S. 2003 The merging of two gaseous bubbles with an application to underwater explosions. *Comput. Fluids* **32**, 1049–1074.

Sapozhnikov, O. A., Khokhlova, A., Bailey, M. R., Williams J R., McAteer, J. A., Cleveland, R. O. & Crum, L. A. 2002 Effect of overpressure and pulse repetition frequency on cavitation in shock wave lithotripsy. *J. Acoust. Soc. Am.* **112**, 1183–1195.

Soh, W. K. & Willis, B. 2003 A flow visualization study on the movement of solid particles propelled by a collapsing cavitation bubble. *Exp. Therm. Fluid Sci.* **27**, 537–544.

Tanguay, M. & Colonius, T. 2003 Progress in modeling and simulation of shock wave lithotripsy (SWL). *Fifth Intl Symp. on Cavitation, Osaka, Japan, November 1–4, 2003.*

Wang, Q. X., Yeo, K. S., Khoo, B. C. & Lam, K. Y. 1996 Strong interaction between a buoyancy bubble and a free surface *Theoret. Comput. Fluid Dyn.* **8**, 73–88.

Zheng, Q., Durben, D. J., Wolf, G. H. & Angell, C. A. 1991 Liquids at large negative pressures: water at the homogeneous nucleation limit. *Science* **254**, 829–832.

Zijlstra, A. & Ohl, C. D. 2008 On fiber optic probe hydrophone measurements in a cavitating liquid. *J. Acoust. Soc. Am.* **123**, 29–32.